

**Electronic structure of substoichiometric Fe-Al intermetallics**

G. P. Das,\* B. K. Rao, and P. Jena

*Physics Department, Virginia Commonwealth University, Richmond, Virginia 23284-2000*

S. C. Deevi

*Research Development and Engineering Center, Philip Morris, Richmond, Virginia 23234*

(Received 15 January 2002; revised manuscript received 25 June 2002; published 12 November 2002)

The formation energy, nature of bonding, electron density of states, and magnetic properties of  $\text{Fe}_{1-x}\text{Al}_x$  intermetallics have been calculated in the concentration range  $0 \leq x \leq 0.5$  using the tight-binding linearized muffin-tin orbital method and a super unit cell containing 16 atoms. The various concentration ranges are simulated by successively replacing Fe atoms by Al atoms and studying the electronic structure within the density-functional theory and generalized gradient approximation for exchange and correlation. The stability of the  $\text{Fe}_{1-x}\text{Al}_x$  alloys increases monotonically with increasing Al concentration, while the magnetic moment variation reveals exactly the opposite behavior. Stoichiometric FeAl is found to exhibit two nearly degenerate magnetic structures: a nonmagnetic state with zero moment on Fe and a ferromagnetic state with a moment of  $0.75\mu_B$  per Fe atom.  $\text{Fe}_3\text{Al}$ , on the other hand, is ferromagnetic with a calculated moment of  $2.45\mu_B$  at the Fe-I site and  $1.95\mu_B$  at the Fe-II site. The coupling between Fe and Al atoms is antiferromagnetic, although the moment at the Al site is much smaller ( $-0.17\mu_B$ ) than that at the Fe sites. The bonding between Fe and Al atoms is primarily due to the hybridization between the  $3d$  electrons of the former and the  $sp$  electrons of the latter. The bonding has a strong local character in that the coupling is between the nearest neighbor atoms. This is further verified by a calculation using small clusters as models of the bulk structure. The density of states at the Fermi energy is dominated by contributions from the Fe  $3d$  state although its variation with Al is modulated by subtle interaction with Al  $3p$  electrons. The total densities of states at the Fermi energy of  $\text{Fe}_{1-x}\text{Al}_x$  alloys show the same variation as the electrical resistivity, suggesting that the increase and then decrease in resistivity with Al concentration with a peak at 33% Al is purely of electronic origin.

DOI: 10.1103/PhysRevB.66.184203

PACS number(s): 71.15.Mb, 71.20.-b, 75.50.Bb

**I. INTRODUCTION**

Transition metal (TM) aluminides are a well-known class of structural intermetallics that possesses a unique combination of several desirable properties such as a high melting point, oxidation and corrosion resistance, being relatively lightweight, and possessing possible room-temperature ductility. In particular, nickel and iron aluminides, in spite of their structural similarity, display a wide range of electronic, mechanical, transport, and magnetic properties.<sup>1-3</sup> All these properties are basically dictated by the interactions between the Al- $p$  and TM- $d$  bands. The subtle changes in the  $p$ - $d$  hybridization brought about by a variation in Al concentration affect the chemical bonding and phase stability in this family of intermetallic alloys. With increasing Al concentrations, charge transfer from Al to TM sites increases, resulting in a significant ionic contribution to otherwise metallic bonding. This is in contrast with the early  $3d$  TM aluminides, where TM-TM directional bonding is the dominant factor governing their structural stability. For example, the  $\beta$  phase of Fe, Co, and Ni aluminides, that crystallize in a  $B2$  (CsCl) structure, persists over a broad range (34–52 at. % Al for FeAl, 45 to 58 at. % Al for CoAl, and 40–55 at. % Al for NiAl) of composition with very little variation in the lattice constant.<sup>4-6</sup> On going from NiAl to FeAl in this family of isostructural stoichiometric compounds, Caskey *et al.*<sup>4</sup> had reported increases in (a) the electronic heat capacity by a factor of 4.3, (b) the Pauli spin susceptibility by a factor of 48, (c) the electrical resistivity by a factor of 10.2 (5.8) at 4.2

K (300 K), and (d) the thermopower by a factor of 3.5 (2.9) at 4.2 K (300 K), along with a change in sign. These observations can be correlated with the fact that for FeAl the electronic density of states (DOS) at the Fermi level  $n(E_F)$  is a factor of  $\sim 4$  higher than that for NiAl,<sup>7</sup> and there is an increased electronic scattering rate as one goes deeper into the  $d$  band. This is also consistent with Mott's simple two-band  $s$ - $d$  model for TM's, according to which the  $d$  band is a trap with a high DOS, into which the  $s$  electrons may be scattered and lost from the electrical current.<sup>8</sup>

The structural phase diagram of Fe-Al system<sup>9,10</sup> is rather complex. In the Fe-rich side, the two ordered phases  $B2$ :FeAl and  $\text{DO}_3$ : $\text{Fe}_3\text{Al}$  are separated by two-phase regions  $\alpha + B2$  and  $\alpha + \text{DO}_3$ ,  $\alpha$  being the disordered phase. There are two lines of second order transitions meeting at a tricritical point. The presence of magnetic ordering makes the situation even more complicated.<sup>11</sup> The magnetic phase diagram<sup>12,13</sup> shows paramagnetic, ferromagnetic and spin-glass regions, which meet at a multicritical point near a  $\sim 30\%$  Al concentration.  $\text{Fe}_{1-x}\text{Al}_x$  solid solutions are ferromagnetic in the concentration range  $0 \leq x < 0.2$ , and the mean magnetic moment (per atom) decreases with Al concentration as per (roughly) the dilution law  $\bar{M} = (1-x)M_{\text{Fe}}$ . Ordered  $\text{Fe}_3\text{Al}$  is also ferromagnetic with  $\bar{M} = 1.4\mu_B$ ,<sup>14</sup> which is less than the dilution law prediction ( $\sim 1.65\mu_B$ ). The magnetic moments per Fe atom are found to be approximately independent of Al content.<sup>5,11</sup> For  $x \geq 0.3$ , ferromagnetic order apparently starts disappearing due to a competi-

tion between nearest-neighbor Fe-Fe ferromagnetic exchange and an indirect Fe-Al-Fe antiferromagnetic superexchange.<sup>13</sup> Although perfectly ordered FeAl is known to be nonmagnetic down to 1 K,<sup>4</sup> disordered (cold-worked) FeAl has been reported to exhibit a magnetic moment of  $0.65\mu_B$ .<sup>5</sup> Interestingly almost all *ab initio* electronic structure calculations in ordered FeAl reveal a magnetic moment of  $\sim 0.7\mu_B$ .<sup>7,15</sup> This controversy, present only in FeAl (but not in isostructural CoAl and NiAl) led to a number of conjectures regarding the role of various point defects and disorder in FeAl in and around stoichiometric compositions. Various unique properties of FeAl, e.g., its ductility, bond strength, and transport and magnetic properties are all rather sensitive to the presence of intrinsic and extrinsic defects.<sup>16–18</sup> Because of the presence of intrinsic disorder in these systems even at exact stoichiometry, Fermi surface measurements like de Haas–van Alphen or cyclotron resonance are ruled out. However, extensive experimental measurements have been carried out on heat capacity, electron momentum density, optical, transport, and magnetic properties, especially on the two ordered phases viz. B2-structured FeAl and DO<sub>3</sub>-structured Fe<sub>3</sub>Al. It is interesting to see how the cohesive, electronic, transport, and magnetic properties change with Al concentration in going from Fe<sub>3</sub>Al to FeAl.

Recently Lilly *et al.*<sup>19</sup> observed a monotonic increase in the electrical resistivity  $\rho_{el}$  of Fe-Al alloy from 0 at. % (pure Fe) to  $\sim 33$  at. % Al, after which there is a rather steep decrease with a further increase in Al concentration. On approaching a 50:50 concentration from the Fe-rich side, a similar monotonic decrease in  $\rho_{el}(x)$  was earlier reported<sup>4</sup> for FeAl, while in the case of isostructural NiAl and CoAl there was a reversal of slope at  $x=0.5$ . Assuming that the underlying crystal structure remains unchanged in this entire range of composition, the authors of Ref. 19 gave a qualitative explanation of this anomaly based on the phenomenological *s-s* and *s-d* scattering theory of Mott and Jones<sup>20</sup> for AB alloys. In FeAl alloys, the Al-3*s* and Fe-3*d* orbitals lie quite close in energy, while Al-3*p* orbitals lie at higher energy. With increasing Al concentration, one would expect more and more charge to be transferred from Al-3*p* to Fe-3*d* until the latter is completely filled. The critical concentration  $x_c$  at which the *d* band can be filled is estimated<sup>21</sup> to be around 0.4, assuming a rigid band model where Al donates three electrons to the Fe 3*d* band. Recall that the peak in the experimental resistivity occurs at  $x\sim 0.33$ .

Reddy and co-workers<sup>21</sup> attempted to understand the change in the electronic structure of iron aluminides by using a finite-size (15-atom) cluster model of Fe<sub>15–*n*</sub>Al<sub>*n*</sub> ( $n=0–7$ ) and performing density-functional calculations. While the electron density of states calculated using the cluster model was consistent with the above charge-transfer model, it failed to bring out the band effects that are reflected in the hybridization strength, solid solution, and long-range behavior in a realistic binary alloy. In addition, a small cluster used to model the bulk has the inherent difficulty that most of the atoms belong to the surface. Several band structure calculations have been performed on Fe-Al alloy systems to investigate their ground- as well as excited-state properties.<sup>7,22–31</sup> However, no attempts have been made to

calculate the concentration dependence of the band structure of these intermetallics far away from stoichiometry.

Here we have attempted a systematic theoretical investigation of the electronic, magnetic and cohesive properties of Fe<sub>1–*x*</sub>Al<sub>*x*</sub> alloys for  $0\leq x\leq 0.5$  using first-principles density-functional calculations with nonlocal gradient correction. The local bonding character has been further explored by using a real-space cluster model. In Sec. II we describe our theoretical procedure. The results are discussed in Sec. III. A summary of our conclusions is given in Sec. IV.

## II. COMPUTATION

A theoretical understanding of the electronic structure and energetics of Fe<sub>1–*x*</sub>Al<sub>*x*</sub> alloys as an Fe atom is replaced by an Al atom using band-structure methodology requires the construction of a super unit cell that includes the Al defects. Ideally this supercell should be large enough that the interaction between the “defects” is minimized. Second, as one increases the defect concentration, it is also necessary to maintain the same supercell so that no additional errors are introduced due to different supercell sizes corresponding to different defect concentrations. Since the computing cost increases substantially with the size of the supercell, a compromise has to be reached between accuracy and efficiency. Therefore, we first discuss the construction of the supercell that will enable us to calculate the band structure, density of states, and cohesive energies of Fe<sub>1–*x*</sub>Al<sub>*x*</sub> alloys for  $0\leq x\leq 0.5$ . We then briefly outline the salient features of our supercell band structure calculations using the linearized muffin-tin orbital (LMTO) method.<sup>32</sup> Finally we discuss a cluster model that enables us to probe the local bonding character between Fe and Al atoms in real space that can be compared with the information gathered from band structure calculation.

### A. Construction of the supercell

The DO<sub>3</sub> structure of Fe<sub>3</sub>Al is shown in Fig. 1. Here each Al atom has eight nearest neighbor (n.n.) Fe atoms (type I), six second n.n. Fe atoms (type II), and 12 third n.n. Al atoms. By replacing all the type-II Fe atoms by Al one obtains the B2 phase of FeAl, while by replacing the Al atoms with Fe one retrieves the bcc Fe structure. Therefore, in our investigation, we have used a 16-atom DO<sub>3</sub> cage in which we have selectively replaced the Fe sites by Al sites, and vice versa, and thereby generated super cells that model substoichiometric Fe<sub>1–*x*</sub>Al<sub>*x*</sub> intermetallic alloys for different values of concentration  $x(0\leq x\leq 0.5)$ . In Table I we list the Fe sites replaced by Al for each concentration  $x$ .

It is to be noted that all the supercells corresponding to the compositions Fe<sub>16</sub>Al<sub>0</sub>, Fe<sub>15</sub>Al<sub>1</sub>, Fe<sub>13</sub>Al<sub>3</sub>, Fe<sub>12</sub>Al<sub>4</sub>, Fe<sub>11</sub>Al<sub>5</sub>, Fe<sub>9</sub>Al<sub>7</sub>, and Fe<sub>8</sub>Al<sub>8</sub> are chosen to be of the *same* size and symmetry (cubic), so that systematic errors can be eliminated. Only site substitutions have been changed to simulate various off-stoichiometric compositions, but they have not been randomized unlike in a truly disordered alloy.<sup>33,34</sup> Note that the earlier supercell calculations<sup>25,31</sup> performed on off-stoichiometric Fe<sub>5</sub>Al<sub>3</sub>, Fe<sub>9</sub>Al<sub>7</sub>, etc. alloys de-

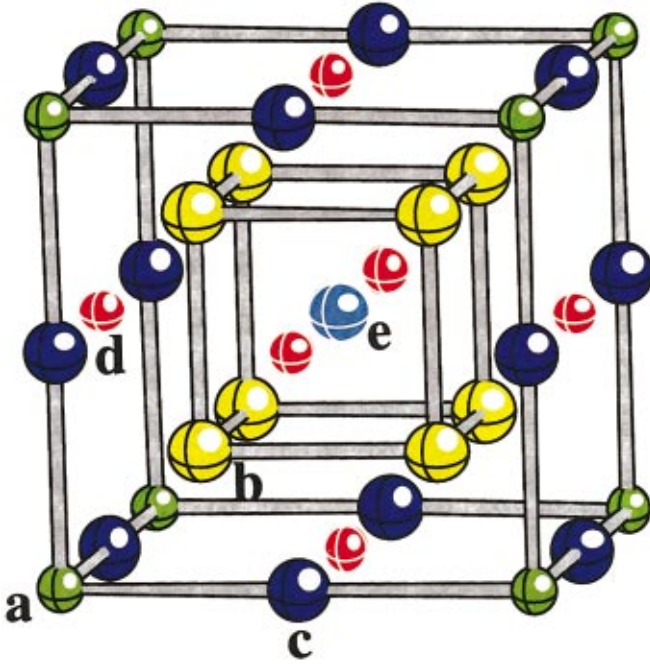


FIG. 1. (Color) Geometrical model of DO<sub>3</sub> structured Fe<sub>3</sub>Al. **a** and **d** are Al sites, **b** is an Fe-I site, while **c** and **e** are Fe-II sites. *ab*, *ac*, *ad*, and *ae* are, respectively, the first-, second-, third-, and fourth-nearest-neighbor distances.

ployed supercells whose symmetry and cell distance were varied. The present model allows us to perform and compare self-consistent total-energy calculations in **k** space under identical conditions, e.g., Brillouin-zone integration and other convergence criteria, as discussed in Sec. II B. Furthermore, in view of the fact that the experimental lattice parameters of Fe<sub>1-x</sub>Al<sub>x</sub> alloys vary marginally, from 2.87 Å for *x* = 0 to 2.92 Å for *x* = 0.5,<sup>5</sup> we have assumed for the lattice constant a value of 2.89 Å in all our calculations. This is consistent with the experimental lattice constant of DO<sub>3</sub>:Fe<sub>3</sub>Al structure.<sup>11</sup> Although, strictly speaking, one would perform energy-volume minimization to estimate the equilibrium lattice constants for each composition; we have purposely avoided this in our present calculations.

## B. Band structure

All the band-structure calculations reported in this work have been performed using self-consistent scalar relativistic tight-binding (TB)-LMTO method in the atomic sphere approximation (ASA),<sup>35,36</sup> based on density-functional theory (DFT). We have also incorporated “combined corrections” (CC) terms that account for the non-sphericity of the atomic Wigner-Seitz-type cells into which the lattice cells can be partitioned. In this approach one uses a minimal basis set and it involves an approximate (overlapping sphere) representation of the potential in the interstitial region. The one-electron potential entering the Schrödinger equation is a superposition of overlapping spherical potential wells with position **R** and radii *S<sub>R</sub>*, plus a kinetic-energy error proportional to the fourth power of the relative sphere overlap.<sup>32</sup> The ASA, in addition, forces the charge density entering Poisson’s equation inside the spheres to be spherical, and it neglects the charge outside the spheres. The Coulomb energy is calculated for a spheridized charge density, and hence the total ground-state energy is not accurate enough to estimate structural energy differences or frozen phonons that require symmetry lowering displacements of atoms.<sup>36</sup> However, the ASA+CC method has proven extremely useful for structures where a close packing of spheres at high-symmetry positions is possible. This is because of the fact that the kinetic-energy error of the ASA+CC method is negligible for a slightly overlapping muffin-tin potential. One needs to know how one can fix the sphere radii for Al and Fe atoms in the present case of a DO<sub>3</sub> caged Fe<sub>1-x</sub>Al<sub>x</sub> supercell. We use the so-called Hartree potential plot prescription.<sup>37</sup> Basically we plot only the Hartree part of the neutral atom potentials for Fe and Al atoms in their respective positions, and then trace the maxima (or saddle-points in three dimensions). For a given atom, the distance to the closest maximum from its center is taken to be its touching sphere radius (since it usually touches the sphere of the neighboring atoms). Subsequently the ASA radii were obtained by inflating these atom-centered touching spheres until they ensure space filling via a permissible overlap, which is defined as

$$w_{RR'} = 1/d[s_R + s_{R'} - d] \times 100 \quad \text{where } d = |\mathbf{r} - \mathbf{R}'|$$

TABLE I. Supercells for stoichiometric and off-stoichiometric Fe<sub>1-x</sub>Al<sub>x</sub> alloys. Sites (a)–(e) are as given in Fig. 1.

Alloys	Al conc. (%)	Site occupancy of Al for each concentration studied				
		Corner site (a) (0,0,0)	Small cube center site (b) (1/4,1/4,1/4)	Edge-center site (c) (1/2,0,0)	Face-center site (d) (1/2,1/2,0)	Body-center site (e) (1/2,1/2,1/2)
Fe <sub>16</sub> Al <sub>0</sub>	0.0	Fe	Fe <sub>1</sub>	Fe <sub>2</sub>	Fe <sub>2</sub>	Fe <sub>2</sub>
Fe <sub>15</sub> Al <sub>1</sub>	6.25	Al	Fe <sub>1</sub>	Fe <sub>3</sub>	Fe <sub>2</sub>	Fe <sub>4</sub>
Fe <sub>13</sub> Al <sub>3</sub>	18.75	Fe	Fe <sub>1</sub>	Fe <sub>3</sub>	Al	Fe <sub>4</sub>
Fe <sub>12</sub> Al <sub>4</sub>	25.0	Al	Fe <sub>1</sub>	Fe <sub>3</sub>	Al <sub>1</sub>	Fe <sub>4</sub>
Fe <sub>11</sub> Al <sub>5</sub>	31.25	Al	Fe <sub>1</sub>	Fe <sub>3</sub>	Al <sub>1</sub>	Al <sub>2</sub>
Fe <sub>9</sub> Al <sub>7</sub>	43.75	Al	Fe <sub>1</sub>	Al <sub>2</sub>	Al <sub>1</sub>	Fe <sub>4</sub>
Fe <sub>8</sub> Al <sub>8</sub>	50.0	Al	Fe <sub>1</sub>	Al <sub>2</sub>	Al <sub>1</sub>	Al <sub>3</sub>

TABLE II. Potential parameters for *B2* FeAl ordered intermetallic.

	Al			Fe		
	<i>s</i>	<i>p</i>	<i>d</i>	<i>s</i>	<i>P</i>	<i>d</i>
$E_v$ (Ry)	-0.4522	-0.2131	-0.1216	-0.3935	-0.2407	-0.0692
$C$ (Ry)	-0.4901	0.3770	1.5758	-0.1743	0.8449	0.0097

For the ASA to work in a reasonable fashion, this overlap value should not increase beyond 15–18% between real atoms. This entire technical procedure for fixing the atomic sphere radii has been automated in the latest version of the Stuttgart TB-LMTO code,<sup>35</sup> which in the present case yields different radius values for Fe-I (*b* site in Fig. 1) and Fe-II (*c* and *e* sites in Fig. 1) which see different environments. The resulting radii for Fe-I, Fe-II, and Al spheres are 2.67, 2.70, and 2.70 a.u., respectively. The Fe-I spheres occupying the small cube centers (tetrahedral positions) turn out to be slightly ( $\sim 1\%$ ) smaller. It is to be noted that unlike in the case of  $\text{La}_2$  and  $\text{CeI}_2$  (in Ref. 36, which are  $\text{Ti}_2\text{Cu}$  intermetallic structure), here we do not need to introduce any empty spheres in the DO3 structure, which are reasonably “close packed.” Also it is to be noted that in all our supercells, we have ensured to use the same average Wigner-Seitz radii (2.688 a.u.) and the same relative radii of the individual spheres, so that the systematic errors get cancelled.

It is well known<sup>38</sup> that the reliability of local spin density (LSD) approximation to the DFT is due to its first-principles character and because it satisfies the constraints for exchange-correlation (XC) hole exactly, resulting in the correct mapping of the ground-state many-body effects from the uniform electron gas to real atoms, molecules, and solids. However, for many real systems such as *3d* transition metals, it has been found that the so-called “gradient corrections” improve the LSD results for the ground-state cohesive and magnetic properties, provided the generalized gradient approximation (GGA) functional also obeys the exact XC hole constraints. Bagno *et al.*<sup>39</sup> compared the effects of different local as well as nonlocal XC potentials, and performed a case study on Fe whose correct ferromagnetic bcc ground state comes out only when Langareth-Mehl-Hu<sup>40</sup> or Perdew-Wang<sup>41</sup> nonlocal functional are used. Recently Lechermann *et al.*<sup>42</sup> compared LSDA and GGA calculations on stoichiometric  $\text{Fe}_3\text{Al}$  and discussed the inadequacy of some of the commonly used GGA functionals in predicting the correct ground state. Although these authors themselves remarked on the apparent disagreement of some of their results with the earlier work by Watson and Weinert,<sup>29</sup> this brings out the subtlety in using different exchange-correlation potentials for a coherent description of the electronic and magnetic properties of this family of transition-metal aluminide system. In the present work, we have used the original Perdew-Wang formulation which is a first-principles nonlocal or rather “semilocal” functional (see Ref. 43 for a detailed derivation and discussion) that is easy to implement.

For all the supercells corresponding to different compositions, we have performed spin-polarized calculations with minimal basis set consisting of *s*, *p*, and *d* orbitals ( $l=2$ ) for

both Fe and Al and using the downfolding procedure.<sup>44</sup> The typical values of the  $E_v$  and  $C$  parameters<sup>36</sup> for *B2*:FeAl are given in Table II. From the  $C$  parameters, which denote the center of gravity of the *l* band, it is seen that Al-*d* band is lying very high in energy (more than a Rydberg); still it has finite hybridization in the aluminide bands. Accordingly, while the Al-*3s* and *3p* and Fe-*3d* and *4s* orbitals have been included as “low” orbitals (occupied), the Al-*d* orbitals have also not been thrown away. These have been treated as “intermediate” orbitals and have been downfolded.<sup>37</sup> This downfolding procedure is especially useful for large supercells, as it helps in reducing the size of the secular matrix and avoids any ghost bands. The core orbitals are kept frozen to their isolated atomic form. No lattice relaxation effects have

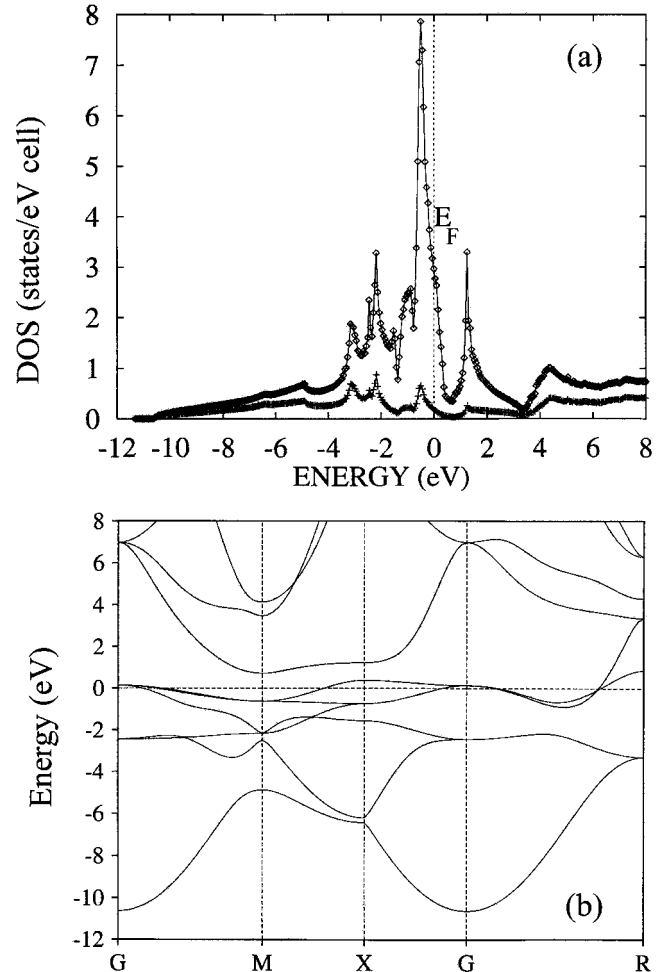


FIG. 2. (a) Total (diamond) and Al-projected (cross) densities of states and (b) band structures of *B2*:FeAl in the paramagnetic state.

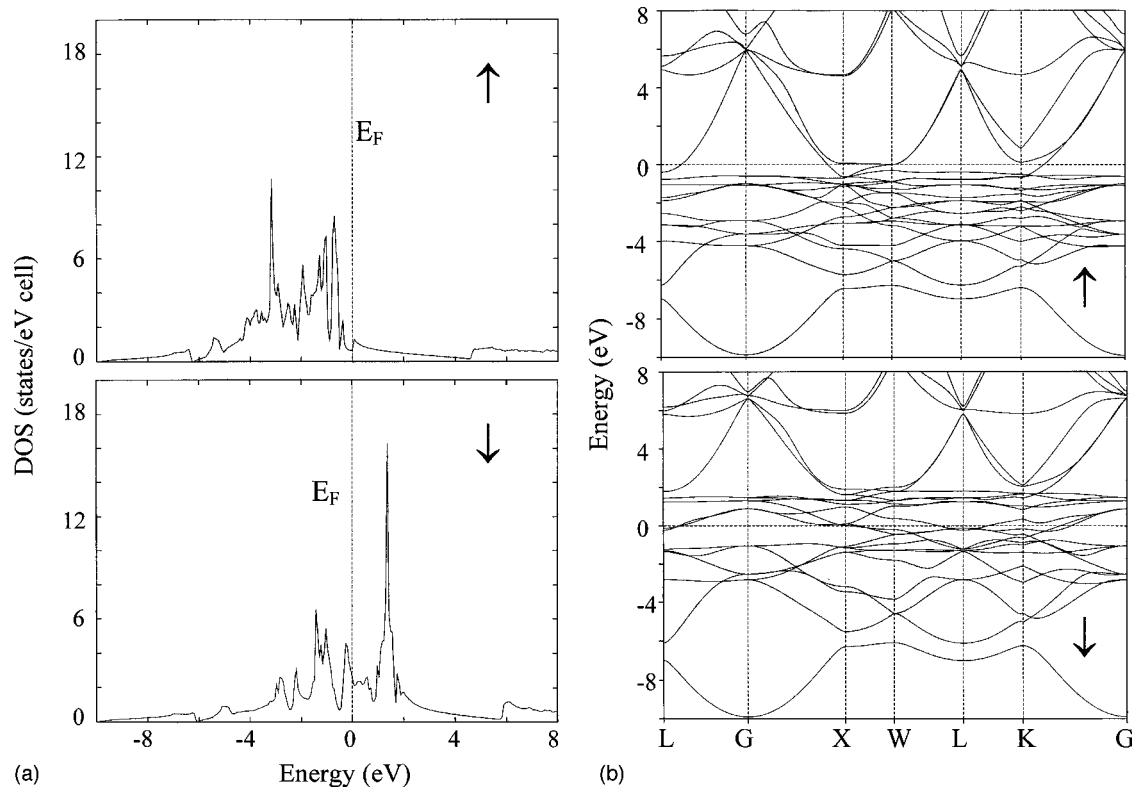


FIG. 3. (a) Densities of states and (b) band structures of  $\text{DO}_3:\text{Fe}_3\text{Al}$  for up ( $\uparrow$ ) and down ( $\downarrow$ ) spins.

been taken into account. Brillouin-zone (BZ) integration has been performed using the tetrahedron method in its latest implementation,<sup>45</sup> which yields proper weighting and corrects errors due to linear approximation of bands inside each tetrahedron. We have used a (10, 10, 10)  $\mathbf{k}$  mesh in all our supercell calculations, which correspond to 56  $\mathbf{k}$  points in the irreducible wedge of the simple cubic BZ (i.e.,  $\frac{1}{48}$ th of the reciprocal primitive cell). All calculations are done semirelativistically, i.e., without taking into consideration spin-orbit interactions which are not significant for  $3d$  transition-metal aluminides. In order to accelerate convergence of our charge self-consistent supercell calculations we use the modified Broyden mixing scheme.<sup>46</sup> However, when we come close to self-consistency we quite often have to take recourse to linear mixing with a very small mixing parameter, in order to take care of the small intersphere charge fluctuations.

In order to understand the nature of bonding in these alloy systems, the so-called “fat bands”<sup>37</sup> are very useful. The fat bands are nothing but the same band structure projected onto different site-orbitals, such as Al- $p_z$  or Fe- $t_{2g}$  or Fe- $e_g$  orbitals. Here each band is allocated a width proportional to the (sum of the) weight(s) of the corresponding orthonormal orbital(s). This is particularly useful to pinpoint the character of the bands that cross the Fermi level, which essentially dictate the bonding, transport, and other properties.

### C. Cluster calculation

In order to augment our understanding of the nature of bonding between Fe and Al derived from the study of fat bands, we have performed cluster calculations for FeAl and

$\text{Fe}_3\text{Al}$  using the molecular orbital approach. Since these are real space calculations, an analysis of the highest occupied molecular orbitals (HOMO's) can illustrate the nature of the bonding between nearest-neighbor atoms. We have modeled the  $B2$  phase of FeAl and the  $\text{DO}_3$  phase of  $\text{Fe}_3\text{Al}$  with the simplest possible cluster geometries that retain only the nearest neighbor Fe-Al interactions. Both are nine-atom clusters in bcc geometry: For FeAl we consider eight Al atoms occupying vertices and one Fe atom in the center, while for  $\text{Fe}_3\text{Al}$  we consider four Al and four Fe atoms occupying alternate vertices and one Fe atom in the body center. In each case the length of the cube edge was fixed at the lattice constant of the corresponding bulk material. The calculations were performed using density-functional theory with generalized gradient approximation as prescribed by Becke, Perdew, and Wang (BPW91).<sup>43,47</sup> The molecular orbitals were represented by linear combinations of atomic orbitals formed out of a double zeta quality numerical basis augmented by the addition of polarization functions. Frozen core approximation was used with this basis set. Spin-polarized calculations were performed using the DMOL software with the spin optimization done through the *aufbau* principle. This computational method has already proved to be effective in providing a qualitative understanding of the electronic structure of bulk systems.<sup>48</sup>

## III. RESULTS

### A. Electronic structure of Fe, Al, FeAl, and $\text{Fe}_3\text{Al}$

In order to establish the reliability of our computational procedure, we first perform self-consistent spin-polarized

TABLE III. Calculated bulk values for ordered Fe-Al intermetallics.

Quantity	<i>B2</i> : FeAl	DO <sub>3</sub> : Fe <sub>3</sub> Al
Lattice Constant (a.u.)	5.46	10.92
Total energy (Ry)	-3032.9859	-8126.3336
Formation energy (eV)	1.63	0.87
$n(E_F)$ states/cell/eV	2.95	16.20
Magnetic moment ( $\mu_B$ ) per Fe atom	0.75	2.06

total-energy band calculations for pure bcc-Fe, fcc-Al, *B2*:FeAl, and DO<sub>3</sub>:Fe<sub>3</sub>Al using the 16-atom supercell and their respective experimental lattice constants. For fcc-Al we see the typical parabolic DOS with a high Fermi-level state density characteristic of the free-electron-like behavior and nearly spherical Fermi surface, while for Fe, we find the  $e_g$ - $t_{2g}$  splitting with Fermi level falling in the “pseudogap,” characteristic of a transition metal. The calculated magnetic moments of Fe for the experimental Fe lattice constant (2.87 Å) and for the experimental Fe<sub>3</sub>Al (5.78 Å) lattice constant are found to be  $2.39\mu_B$  and  $2.48\mu_B$  respectively. It is to be noted that these values are slightly higher than those calculated using the LSD approximations, mainly due to the fact that the nonlocal corrections favor larger magnetic polarization. On inflating the Fe lattice constant, its magnetic moment increases, but the Fermi-level state density decreases because of the slight shifting of the Fermi level on the falling edge of the bonding peak in the DOS.

For the bulk FeAl and Fe<sub>3</sub>Al calculations, we have used 286 and 413 nonequivalent  $k$  points, respectively, in the irreducible BZ, and ensured  $k$  mesh convergence. The DOS and band structures of FeAl and Fe<sub>3</sub>Al are shown in Figs. 2 and 3 for the energy range of  $\pm 10$  eV with respect to Fermi level which is chosen to be zero all throughout this work. The normal bands of bulk FeAl or Fe<sub>3</sub>Al are plotted along the high symmetry directions of the cubic BZ  $\Gamma \rightarrow X \rightarrow W \rightarrow L \rightarrow K \rightarrow \Gamma$ . The Fermi level lies at the steeply falling edge of the bonding peak in the density of states. The relative contribution from Al sublattice is found to be rather small. Figures 3(a) and (b) show the energy bands and DOS's for spin-up and -down electrons of Fe<sub>3</sub>Al. These results match with the published theoretical calculations.<sup>7</sup> Our calculated DOS's of FeAl and Fe<sub>3</sub>Al also compare well with the experimental photoelectron spectra. In particular, the Fermi level state densities that dictate most of the transport properties are in good agreement. Charge transfer in a metallic system is a poorly defined quantity due to the inherent ambiguity in partitioning of charge especially within the ASA. Nevertheless, one can adapt some consistently defined intersphere charge transfer, for example, the incremental addition of one charge while going across a series of *B2* structured transition metal aluminides having the same sphere radii.<sup>7,49</sup> Using a similar prescription in the present case, we have estimated the charge transfer from Al to Fe to be  $\sim 0.2$  electrons in FeAl, which is small compared to those in other Fe-rich alloys, thereby indicating a higher stability for the *B2* phase.

Table III summarizes the results on cohesive and elec-

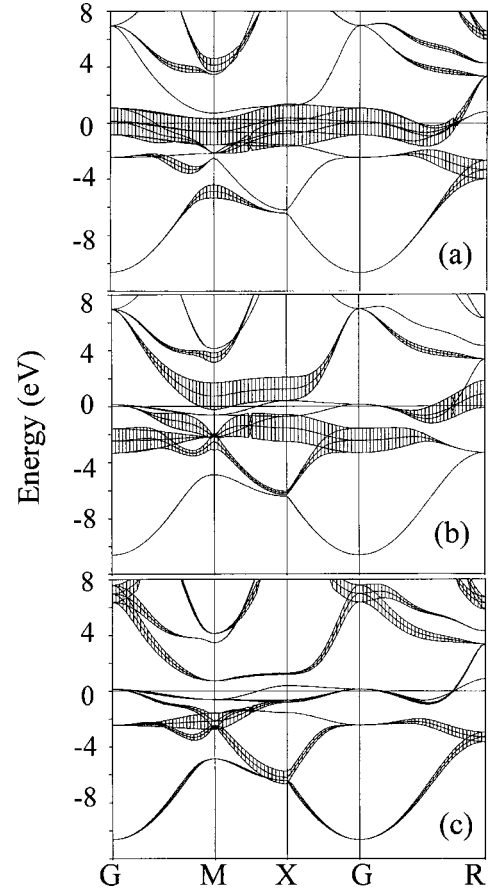


FIG. 4. Projected “fat bands” of *B2*:FeAl projected (a) Fe- $t_{2g}$ , (b) Fe- $e_g$ , and (c) Al- $p$ .

tronic properties of *B2*:FeAl and DO<sub>3</sub>-Fe<sub>3</sub>Al, which are used as references for our subsequent supercell calculations for different Al compositions. The ground-state total energies of bcc-Fe and fcc-Al, i.e.,  $E_{\text{total}}(\text{Fe})$  and  $E_{\text{total}}(\text{Al})$ , have been used in conjunction with the corresponding values for the ordered *B2* and DO<sub>3</sub> phases, to calculate the formation energies of the intermetallics at various Al compositions, namely,

$$E_{\text{form}}(\text{Fe}_{1-x}\text{Al}_x) = E_{\text{total}}(\text{Fe}_{1-x}\text{Al}_x) - [(1-x)E_{\text{total}}(\text{Fe}) + xE_{\text{total}}(\text{Al})].$$

The formation energies, magnetic moments and Fermi-level state densities may be compared with other calculations reported in the literature.<sup>18,29</sup> For example, our calculated magnetic moments are  $2.45\mu_B$  for the Fe-I site and  $1.95\mu_B$  for the Fe-II site, while the corresponding values obtained by Watson and Weinert<sup>29</sup> are  $2.21\mu_B$  and  $1.59\mu_B$ , respectively. They also estimated the formation energy  $\Delta H$  for FeAl to be almost twice that of Fe<sub>3</sub>Al, which is in agreement with the factor of 2 higher value for FeAl formation energy that we obtain (see Table II). However, such an agreement turns out to be rather fortuitous, since our absolute values for the formation energies are very different from those of Watson and Weinert. This may be due to several factors, e.g., Watson and Wienert performed full potential calculations using the local-

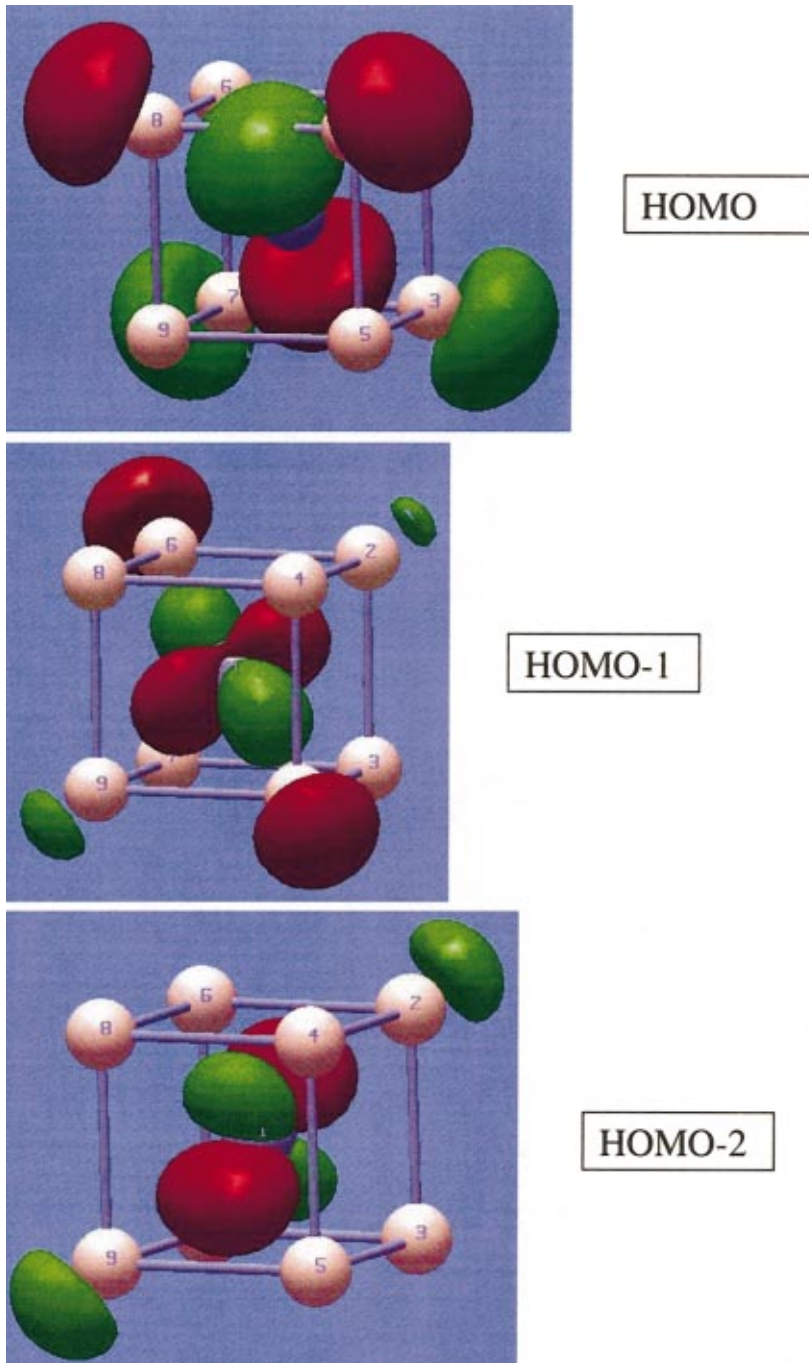


FIG. 5. (Color) HOMO, HOMO-1, and HOMO-2 orbitals of  $B_2:FeAl$ .

spin-density approximation, while ours is done with the ASA and includes gradient correction; this leads to different error bars in the atomic calculations. Furthermore, they performed energy minimization to obtain the equilibrium lattice constant for each structure, whereas we have purposely kept the lattice constant fixed (at the experimental value for  $DO_3$ -structured  $Fe_3Al$ ) for reasons mentioned in Sec. II A.

For  $B_2$ - $FeAl$  we have shown (Fig. 4) the fat bands corresponding to  $Fe-t_{2g}$ ,  $Fe-e_g$ , and  $Al-p$  orbitals. It is clear that the bands crossing the Fermi level are predominantly  $Fe-t_{2g}$ , while  $Fe-e_g$  bands are just above or below (and sometime touching) the Fermi level. The  $Al-p$  bands, on the other hand, make small contribution, although they do hy-

bridize with the  $Fe-t_{2g}$  bands. These results are also reflected in our cluster calculation performed on a nine-atom  $Fe_8Al$  cluster (with only nearest neighbor  $Fe-Al$  interaction) in bcc geometry. In Fig. 5 we plot the  $p$ - and  $d$ -lobes of the highest occupied molecular orbital and also those corresponding to HOMO-1 and HOMO-2 orbitals. Note that the bonding between  $Al-p$  and  $Fe-d$  orbitals are evident from large  $t_{2g}$  lobes of the central  $Fe$  atom pointing toward the  $p$  lobes of the corner  $Al$  atoms. In the case of  $DO_3:Fe_3Al$  the bands are more complicated because of the existence of two different types of  $Fe$  (types I and II), and correspondingly there are more number of  $Fe-Al$  bonds. The bands around the Fermi level are predominantly  $Fe-e_g$  bands. Figure 6 shows the  $e_g$

bands corresponding to Fe-I and Fe-II atoms, the former (i.e., the n.n. Fe atoms) making a larger contribution as expected. The Al- $p$  contribution, on the other hand, is negligible (not shown in Fig. 6). The cluster calculations performed on the nine-atom cluster (representing the smallest possible cluster for the  $\text{DO}_3\text{:Fe}_3\text{Al}$  structure as discussed in Sec. II C) shows the essential bonding nature for the HOMO and the two orbitals below the HOMO. The results are given in Fig. 7. The  $p$  orbitals of the Al atoms interact with the  $d$  lobes of the Fe atom at the center of the cube, while the  $d$  orbitals of the cube corners do not participate as much.

### B. Electronic structure of $\text{Fe}_{1-x}\text{Al}_x$

The salient features of the electronic structure of the substoichiometric  $\text{Fe}_{1-x}\text{Al}_x$  alloys emerge from their total, as well as site-projected DOS, shown in Fig. 8. First of all, the DOS's of  $\text{Fe}_{16}\text{Al}_0$ ,  $\text{Fe}_{12}\text{Al}_4$ , and  $\text{Fe}_8\text{Al}_8$  supercells, which correspond to stoichiometric compositions, match almost exactly with those of bulk Fe,  $\text{Fe}_3\text{Al}$ , and FeAl, respectively, thereby suggesting the size convergence of the  $\mathbf{k}$  mesh used in our supercells. Comparing the DOS's of the various supercells in Fig. 8, we observe the following. (a) The DOS at and near Fermi level are governed mainly by Fe. (b) The Fermi level falls in the pseudogap between the bonding and antibonding peaks. (c) As the Al concentration increases, the bonding peak has a tendency to come closer to the Fermi level. (d) The exact location of the Fermi level, i.e., whether it lies on a peak or a valley, or a falling edge within the broad pseudogap crucially depends on the strength of hybridization between Al- $p$  and Fe- $d$ , and the charge transfer from Al to Fe at that particular concentration. It should be pointed out that these features agree qualitatively with the conclusions reached in Ref. 21 using a cluster model for the substoichiometric aluminides. Quantitative estimates of the total DOS at  $E_F$ ,  $n(E_F)$ , and its contributions from the Fe and Al sublattices, are given in Table IV. The formation energies of  $\text{Fe}_{1-x}\text{Al}_x$  alloys as the Al concentration increases are also listed in Table IV. Note that the formation energy calculated using Eq. (1) is found to increase with increasing Al concentration.

We now attempt to interpret the observed anomaly in electrical resistivity  $\rho_{\text{el}}$  of Fe-rich  $\text{Fe}_{1-x}\text{Al}_x$  alloys, based on the results of our electronic structure calculation. The theoretical foundation of the transport properties of metals and alloys, and in particular their electrical resistivities have been extensively dealt with in the literature.<sup>50,51</sup> The electrical resistivity of a metallic  $A_xB_{1-x}$  alloy depends on various factors, as summarized below. First it depends on the type of scattering centers, i.e., whether it is a simple metal characterized by an  $sp$ -band or a transition metal governed mainly by the  $d$  band. Second,  $\rho_{\text{el}}$  depends on the atomic fraction of the impurity  $x$ , namely,

$$\rho_{\text{el}}(x) = m v_F x \tau / e^2,$$

where  $\tau$  is the scattering cross section and  $v_F$  is the Fermi velocity. This simple formula, which suggests that the resistivity is proportional to the Fermi velocity, is strictly true only for a simple monovalent metal. But for transition met-

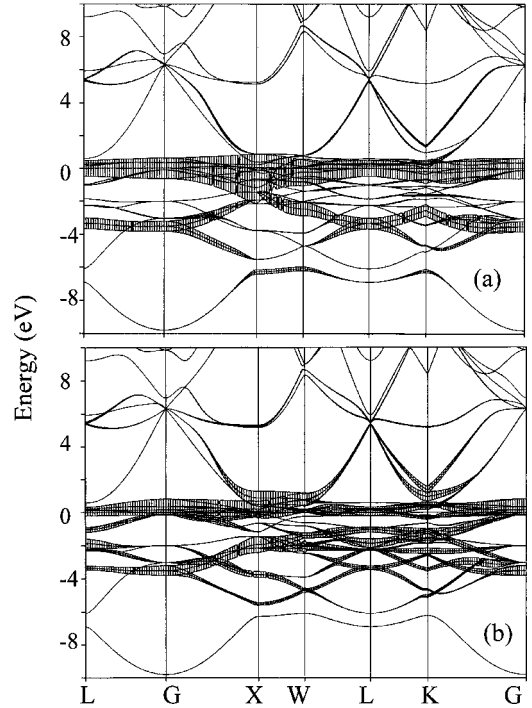
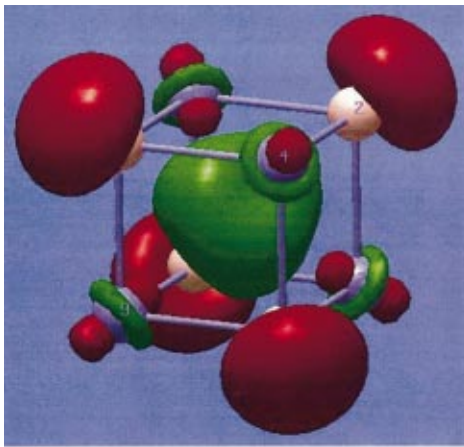
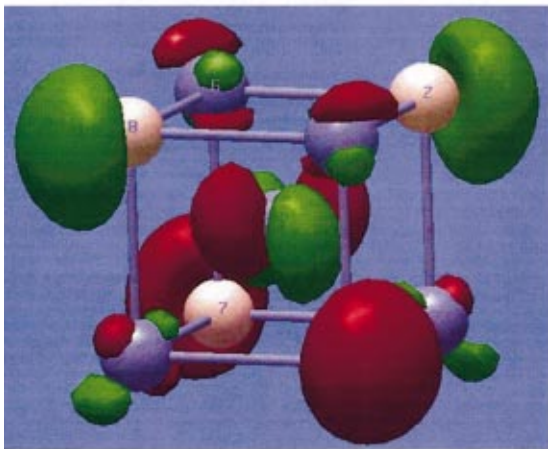


FIG. 6. Fat bands of  $\text{DO}_3\text{Fe}_3\text{Al}$  projected onto  $e_g$  bands of (a) Fe-I and (b) Fe-II.

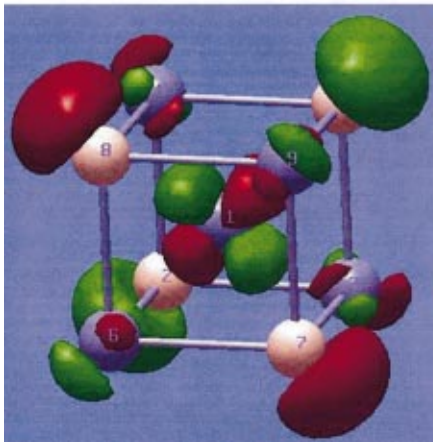
als, the behavior becomes more complex, as it is not clear how to count the relatively localized  $d$  electrons that are near the Fermi surface. Third,  $\rho_{\text{el}}$  depends on whether the alloy is ordered or disordered. The residual resistivity for a perfectly ordered phase is zero, since the regular lattice structure only alters the dynamical properties of electrons and does not cause them to be scattered incoherently.<sup>50</sup> In the case of transition metals, one can divide electrons into two groups; the  $s$  band, with free-electron-like behavior and a nearly spherical Fermi surface (FS); and the  $d$  band, with a lower Fermi velocity ( $v_d \ll v_s$ ) and a complicated FS topology. Since the areas  $A_s(A_d)$  of the FS corresponding to the  $s$  band ( $d$  band) are comparable, the product  $v_d A_d$  is negligible compared to  $v_s A_s$ , implying that most current is actually carried by the  $s$  electrons.<sup>50</sup> The contribution to the electrical resistivity from the  $s$ - $d$  scattering of electrons by phonons turns out to be greater than the  $s$ - $s$  scattering by a factor that is roughly the ratio of the DOS in the  $s$  and  $d$  bands. The simplistic argument put forth by Mott<sup>8</sup> to explain the relatively high resistivity of the TM's was as follows: The localized  $d$  band can be looked upon as a trap with a high DOS, into which the itinerant  $s$  electrons may be scattered and lost from the electric current. For Ag-Pd alloys, the electrical resistivity was found to increase to  $\sim 36$  at. % Ag and then drop down steeply to  $\sim 50$  at. %, after which it goes down with a lesser gradient till it reaches a low value for Ag.<sup>52</sup> Here the monovalent Ag goes on donating its conduction electrons to the unfilled  $d$  band of Pd. But at a certain composition ( $\sim 36$  at. %) the conduction electrons of Ag are no longer sufficient to fill the holes which results in the observed asymmetric peak. This behavior is reminiscent of the resistivity anomaly observed in our present case.



HOMO



HOMO-1



HOMO-2

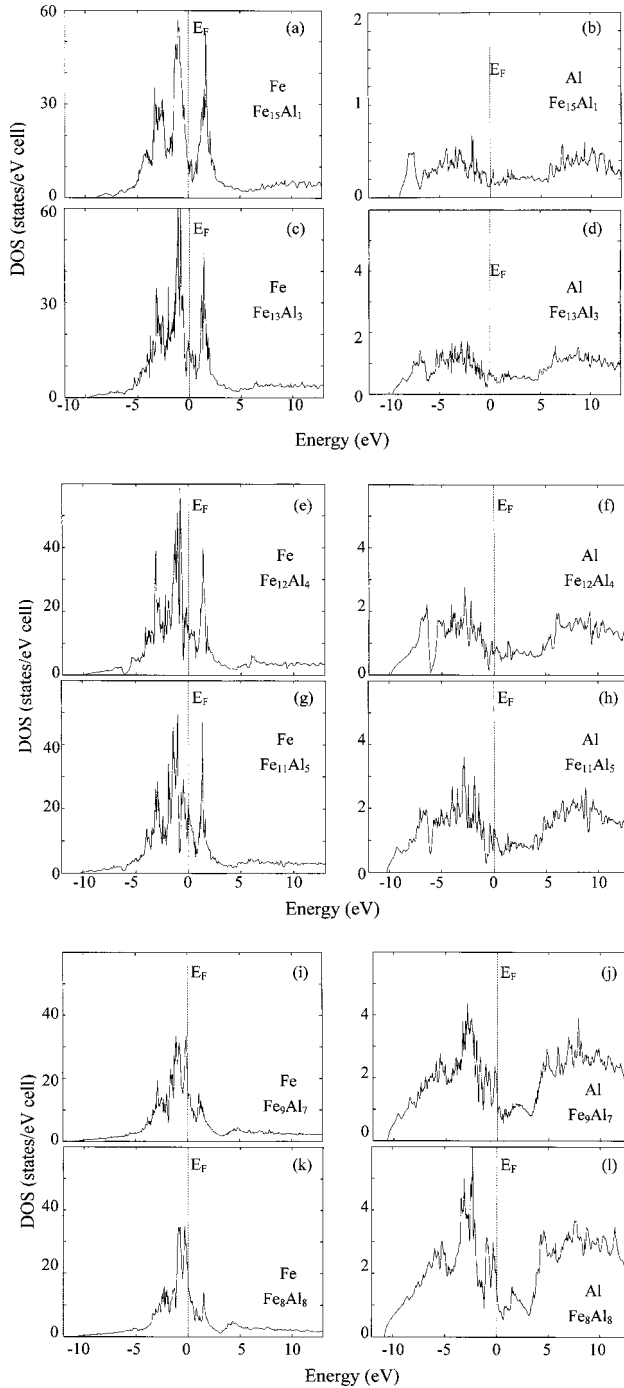
FIG. 7. (Color) HOMO, HOMO-1, and HOMO-2 orbitals of  $\text{DO}_3:\text{Fe}_3\text{Al}$ .

In the present case of FeAl alloys, since one component ( $p$  electrons of Al) is more free-electron-like while the other ( $d$  electrons of Fe) are more localized, it is difficult to separate out their respective contributions to  $\rho_{\text{el}}$ . Accordingly, there is interesting, albeit complicated, interplay between the relatively narrow Fe  $d$  band (i.e., low  $v_F$ ) and broad Al  $sp$  band (i.e., high  $v_F$ ). However, what we have tried to underscore here is the similarity between  $n(E_F)$  and  $\rho_{\text{el}}$  as a function of  $x$ . In fact, we have separated  $n(E_F)$  into  $n^{\text{Fe}}(E_F)$  and  $n^{\text{Al}}(E_F)$ , which are plotted in Fig. 9, so that the  $s$ - $s$  and  $s$ - $d$  scattering contributions to  $\rho_{\text{el}}$  can be seen. As expected, the Fe contribution is an order of magnitude larger than the Al contribution on the Fermi-level state densities. It is interesting to see that both these curves peak at  $x=0.31$  and this is

approximately where the resistivity peak is also observed experimentally by Lilly *et al.*<sup>19</sup> It is to be noted that the  $y$ -scales of these two DOS plots are quite different.

### C. Magnetic properties of $\text{Fe}_{1-x}\text{Al}_x$

Finally, we come to the magnetic properties of this family of  $\text{Fe}_{1-x}\text{Al}_x$  intermetallic alloys. The total magnetic moment  $M_{\text{tot}}$  (Table V) reduces with increasing Al concentration, which is expected as a result of quenching of Fe moment due to overlap with electrons of the Al atoms. For low Al concentration ( $\leq 20$  at. %), the average magnetic moment  $\bar{M} = M_{\text{tot}}/16$  approximately obeys the dilution law. As mentioned in Sec. I, the average magnetic moment in cold

FIG. 8. Fe- and Al-projected DOS's of  $\text{Fe}_{1-x}\text{Al}_x$  supercells.

worked disordered Fe-rich Fe-Al alloys up to 50% concentration had been measured.<sup>5</sup> The values continuously decrease with Al concentration, starting with  $2.2\mu_B$  per atom in pure Fe and going to  $0.32\mu_B$  per atom at a 50:50 concentration. Assuming a linear dependence, this corresponds to a slope  $d\bar{M}/dc = -3.8\mu_B$ , while our calculated slope (Fig. 10) is  $\sim -4\mu_B$ . The reader should, however, be cautioned that the experiment was carried out on disordered system where defects also could play a role. Our calculations, based on supercell geometry, correspond to an ordered system.

TABLE IV. Energy of formation and electronic DOS at  $E_F$  for various  $\text{Fe}_{1-x}\text{Al}_x$  alloys. Here “cell” designates 1/16th of the supercell.

Alloys $\text{Fe}_{1-x}\text{Al}_x$	Formation energy (eV)	$n(E_F)$ (states per eV per “cell”)				
		Total	Al	Fe	Fe-d	Fe-sp
$\text{Fe}_{16}\text{Al}_0$	0.00	16.75	0.0	16.75	16.4	0.3
$\text{Fe}_{15}\text{Al}_1$	-1.068	9.4	0.2	9.2	8.0	1.2
$\text{Fe}_{13}\text{Al}_3$	-2.616	13.2	0.6	12.6	11.5	1.1
$\text{Fe}_{12}\text{Al}_4$	-3.484	13.5	0.7	12.8	11.7	1.1
$\text{Fe}_{11}\text{Al}_5$	-3.653	21.2	1.4	19.8	18.4	1.4
$\text{Fe}_9\text{Al}_7$	-4.786	18.8	1.2	17.6	16.7	0.9
$\text{Fe}_8\text{Al}_8$	-5.721	16.6	1.5	15.1	14.5	0.6

Nevertheless the agreement between our calculation and experiment is worth noting.

Our calculated magnetic moment for  $\text{Fe}_3\text{Al}$  is  $2.06\mu_B$  per Fe atom (taking into account the fact that there are two atoms of Fe-II type, one atom of Fe-I type, and the moment at Al

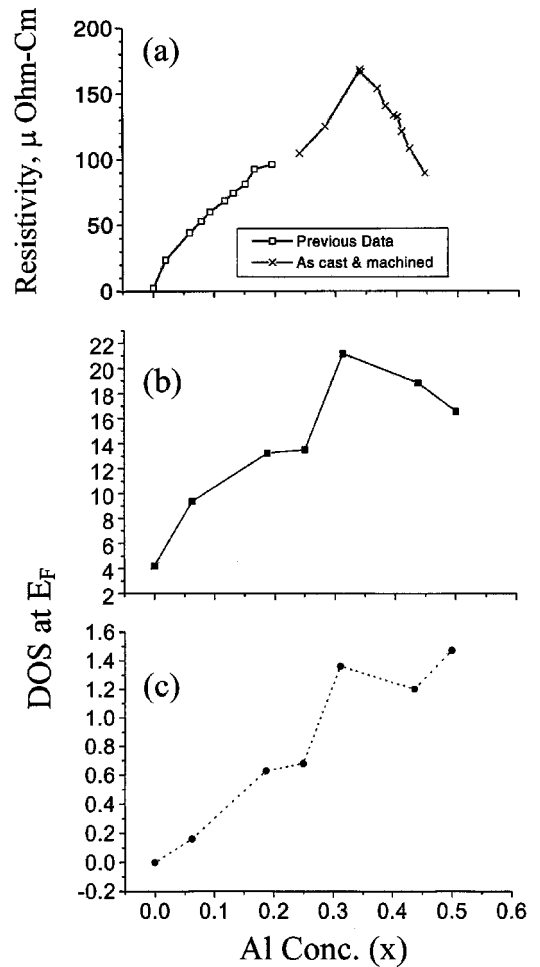


FIG. 9. (a) The experimental resistivity curve (Ref. 16) for  $\text{Fe}_{1-x}\text{Al}_x$  alloys as a function of Al concentration ( $0 \leq x \leq 0.5$ ). Our calculated Fermi-level state densities as functions of  $x$  for (b) total and (c) Al sites.

TABLE V. Local magnetic moments at individual Fe and Al sites in  $\text{Fe}_{1-x}\text{Al}_x$  super cells.

Alloys	Total magnetic moment ( $\mu_B$ )	Site occupancy				
		Corner (a) (0,0,0)	SC-cent (b) (1/4,1/4,1/4)	Edge-cent (c) (1/2,0,0)	Face-cent (d) (1/2,1/2,0)	Body-cent (e) (1/2,1/2,1/2)
$\text{Fe}_{16}\text{Al}_0$	39.52	Fe	Fe	$\text{Fe}_2$	$\text{Fe}_2$	$\text{Fe}_2$
$\text{Fe}_{15}\text{Al}_1$	36.55	Al	$\text{Fe}_1$	$\text{Fe}_3$	$\text{Fe}_2$	$\text{Fe}_4$
$\text{Fe}_{13}\text{Al}_3$	29.13	Fe	$\text{Fe}_1$	$\text{Fe}_3$	Al	$\text{Fe}_4$
$\text{Fe}_{12}\text{Al}_4$	24.74	Al	$\text{Fe}_1$	$\text{Fe}_3$	$\text{Al}_1$	$\text{Fe}_4$
$\text{Fe}_{11}\text{Al}_5$	20.53	Al	$\text{Fe}_1$	$\text{Fe}_3$	$\text{Al}_1$	$\text{Al}_2$
$\text{Fe}_9\text{Al}_7$	10.26	Al	$\text{Fe}_1$	$\text{Al}_2$	$\text{Al}_1$	$\text{Fe}_4$
$\text{Fe}_8\text{Al}_8$	5.98	Al	$\text{Fe}_1$	$\text{Al}_2$	$\text{Al}_1$	$\text{Al}_3$

site is  $-0.17\mu_B$ ), which is in reasonable agreement with the experimental values of  $1.8\mu_B$ .<sup>11</sup> All the supercell calculations were carried out using an  $\text{Fe}_3\text{Al}$  lattice constant which is in between that of pure Fe and B2:FeAl. Thus for pure Fe we obtain magnetic moment of  $2.48\mu_B$ , whereas on using an experimental lattice constant, the magnetic moment comes out to be  $2.39\mu_B$ . Although experimentally no magnetic moment has been found for the well-annealed B2 phase of FeAl, our calculation shows a net magnetic moment of  $0.75\mu_B$  per Fe atom, and this latter value matches what was yielded by other local-density calculations.<sup>7,29</sup> This discrepancy between theory and experiment is rather intriguing. However, it should be pointed out that the ferromagnetic ground state turns out to be only  $\sim 2$  mRy below the paramagnetic one. In view of the  $\sim$ mRy accuracy of our TB-LMTO-ASA total-energy calculation, this difference is rather small. We are therefore inclined to believe that the two states are nearly degenerate, and a very small perturbation may cause a switch over from the ferromagnetic to paramagnetic state, or vice versa. Experimentally also it has been found (as discussed in Sec. I) that the presence of small disorder leads to completely different results. Table V also shows the concentration variation of the local magnetic moments on the individual Fe sites and Al sites in the supercells. Among the Fe sites, the tetrahedral (small-cube center) site always has the minimum moment, while the other Fe sites have higher (but of the same sign) magnetic moments, depending on its number of Al neighbors. The Al atoms are also found to carry very small (induced) magnetic moments of up to  $\sim 0.2\mu_B$  but of opposite sign. This antiferromagnetic coupling between Fe and Al atoms was also found from cluster calculations.<sup>21</sup> The intersphere charge transfer from Al to Fe is found to be at a minimum for  $\text{Fe}_8\text{Al}_8$ , which explains the stability of the B2 phase and the concomitant small magnetic moment.

#### IV. CONCLUSIONS

We have performed first-principles density-functional calculations on substoichiometric  $\text{Fe}_{1-x}\text{Al}_x$  alloys using a supercell geometry and a linearized muffin-tin orbital method. The variation in formation energy and electronic and magnetic properties as a function of Al concentration was calculated. The results, based on density-functional theory and the generalized gradient approximation for exchange and correlation, agree well with existing calculations and experiments on stoichiometric  $\text{Fe}_3\text{Al}$  and FeAl, as well as pure Fe and Al crystals. This agreement validates the choice of our computational procedure. With increasing Al concentration, the magnetic moment decreases due to loss of Fe-*d* charge. While at a 75:25 concentration,  $\text{Fe}_3\text{Al}$  is clearly ferromagnetic with a magnetic moment of  $\sim 2\mu_B$  per Fe atom; at a 50:50 concentration stoichiometric FeAl exists in two nearly degenerate states—a nonmagnetic state which is only 2 mRy higher in energy than the ferromagnetic state. The bonding between Fe and Al atoms is dominated by nearest-neighbor

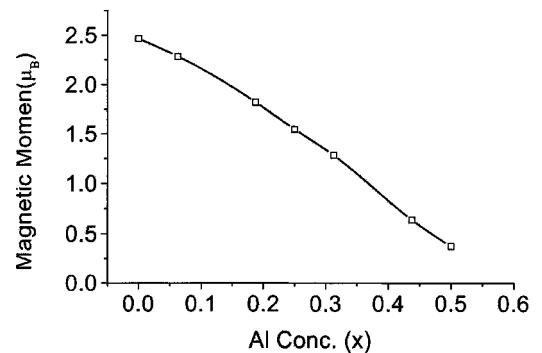


FIG. 10. Average magnetic moments of  $\text{Fe}_{1-x}\text{Al}_x$  supercells as functions of concentration  $x$ .

interaction including hybridization of Fe  $3d$  with Al  $3p$  states. As the Al concentration increases, the antibonding  $p$ - $d$  hybridization increases and so does the total density of states at the Fermi energy, which peaks around  $x \approx 0.33$  and then decreases. This behavior is very similar to the concentration dependence of electrical resistivity in  $\text{Fe}_{1-x}\text{Al}_x$  suggesting that the resistivity anomaly has an electronic origin. These results are consistent with model calculations where atomic clusters are used as model of the bulk. It is also instructive to note that in our model supercell calculations, while the number of Fe-Al bonds increases monotonically from  $\text{Fe}_{16}\text{Al}_0$  to

$\text{Fe}_8\text{Al}_8$ , there is a sudden fall in the number of Fe-Fe bonds when we reach  $\text{Fe}_{11}\text{Al}_5$ . Up to this concentration of  $\sim 33\%$ , the Fe atom experiences a surrounding by eight other Fe atoms, but after this concentration such an Fe-cluster ceases to exist. This is reflected in the electronic structure as well as magnetic properties of this family of  $\text{Fe}_{1-x}\text{Al}_x$  alloys.

#### ACKNOWLEDGMENT

This work was supported in part by a grant from the Department of Energy (DE-FG02-96ER45579).

- \*On leave from Bhabha Atomic Research Center, Mumbai, India.
- <sup>1</sup>R. L. Fleisher, D. M. Dimidick, and H. A. Lipsitt, *Annu. Rev. Mater. Sci.* **19**, 231 (1989).
  - <sup>2</sup>C. T. Liu, J. Stringer, J. N. Mundy, L. L. Horton, and P. Angelini, *Intermetallics* **5**, 579 (1997); also see articles in the special issue of *Mater. Sci. Eng.* **258** (1998).
  - <sup>3</sup>B. V. Reddy and S. C. Deevi, *Intermetallics* **8**, 1369 (2000); S. C. Deevi, V. K. Sikka, and C. T. Liu, *Prog. Mater. Sci.* **42**, 177 (1997); S. C. Deevi and V. K. Sikka, *Intermetallics* **4**, 357 (1996).
  - <sup>4</sup>G. R. Caskey, J. M. Franz, and D. J. Sellmyer, *J. Phys. Chem. Solids* **34**, 1179 (1973).
  - <sup>5</sup>A. J. Besnus, A. Herr, and A. J. P. Meyer, *J. Phys. F: Met. Phys.* **5**, 2138 (1975).
  - <sup>6</sup>D. Singh, in *Intermetallic Compounds*, edited by J. H. Westbrook and R. L. Fleisher (Wiley, New York, 1994), Vol. 2.
  - <sup>7</sup>V. Sundarajan, B. R. Sahu, D. G. Kanhere, P. V. Panat, and G. P. Das, *J. Phys.: Condens. Matter* **7**, 6019 (1995).
  - <sup>8</sup>N. F. Mott, *Proc. Phys. Soc. London* **47**, 571 (1935).
  - <sup>9</sup>S. M. Allen and J. W. Cahn, *Acta Metall.* **23**, 1017 (1975); S. M. Allen, *Philos. Mag.* **36**, 181 (1977).
  - <sup>10</sup>*Binary Alloy Phase Diagrams*, edited by T. B. Massalaski, 2nd ed. (ASM International, Materials Park, OH, 1990).
  - <sup>11</sup>R. Kuentzler, *J. Phys. (Paris)* **44**, 1167 (1983).
  - <sup>12</sup>R. D. Shull, H. Okamoto, and P. A. Beck, *Solid State Commun.* **20**, 863 (1976).
  - <sup>13</sup>P. Shukla and M. Wortis, *Phys. Rev. B* **21**, 159 (1980).
  - <sup>14</sup>T. Wakiyama, *J. Phys. Soc. Jpn.* **32**, 1222 (1972).
  - <sup>15</sup>Using the LDA+U scheme, Mohn *et al.* [P. Mohn, C. Persson, P. Blaha, K. Schwarz, P. Novák, and E. Eschrig, *Phys. Rev. Lett.* **87**, 196401 (2001)] recently found a nonmagnetic ground state for the B2 phase of FeAl.
  - <sup>16</sup>C. L. Fu, Y.-Y. Ye, M. H. Yoo, and K. M. Ho, *Phys. Rev. B* **48**, 6712 (1993).
  - <sup>17</sup>J. Bogner, W. Steiner, M. Reissner, P. Mohn, P. Blaha, K. Schwarz, R. Krachler, H. Ipser, and B. Sepiol, *Phys. Rev. B* **58**, 14 922 (1998).
  - <sup>18</sup>N. I. Kulikov, A. V. Postnikov, G. Borstel, and J. Braun, *Phys. Rev. B* **59**, 6824 (1999).
  - <sup>19</sup>A. C. Lilly, S. C. Deevi, and Z. P. Gibbs, *Mater. Sci. Eng., A* **258**, 42 (1998).
  - <sup>20</sup>N. F. Mott and H. Jones, *The Properties of Metals and Alloys* (Dover, New York, 1958).
  - <sup>21</sup>B. V. Reddy, P. Jena, and S. C. Deevi, *Intermetallics* **8**, 1197 (2000); B. V. Reddy, S. C. Deevi, A. C. Lilly, and P. Jena, *J. Phys.: Condens. Matter* **13**, 8363 (2001).
  - <sup>22</sup>R. Eibler and A. Neckel, *J. Phys. F: Met. Phys.* **10**, 2179 (1980).
  - <sup>23</sup>C. Koenig and M. A. Khan, *Phys. Rev. B* **27**, 6129 (1983).
  - <sup>24</sup>J. M. Koch, N. Stefanou, and C. Koenig, *Phys. Rev. B* **33**, 5319 (1986).
  - <sup>25</sup>Y. M. Gu and L. Fritsche, *J. Phys.: Condens. Matter* **4**, 1905 (1992).
  - <sup>26</sup>G. A. Botton, G. Y. Guo, W. M. Temmerman, and C. J. Humphreys, *Phys. Rev. B* **54**, 1682 (1996).
  - <sup>27</sup>V. N. Antonov, O. V. Krasovska, E. E. Krasovskii, Yu V. Kudryavtsev, V. V. Nemoshkalenko, B. Yu Yavorsky, Y. P. Lee, and K. W. Kim, *J. Phys.: Condens. Matter* **9**, 11227 (1997).
  - <sup>28</sup>S. K. Bose, V. Drachal, J. Kudrnovsky, O. Jepsen, and O. K. Andersen, *Phys. Rev. B* **55**, 8184 (1997).
  - <sup>29</sup>R. E. Watson and M. Weinert, *Phys. Rev. B* **58**, 5981 (1998).
  - <sup>30</sup>B. Meyer and M. Faehnle, *Phys. Rev. B* **59**, 6072 (1999).
  - <sup>31</sup>J. Y. Rhee, *J. Phys.: Condens. Matter* **11**, 8867 (1999).
  - <sup>32</sup>O. K. Andersen, *Phys. Rev. B* **12**, 3060 (1975).
  - <sup>33</sup>I. Dasgupta, T. Saha-Dasgupta, A. Mookerjee, and G. P. Das, *J. Phys.: Condens. Matter* **9**, 3529 (1997).
  - <sup>34</sup>G. P. Das, in *Frontiers in Materials Modelling and Design*, edited by V. Kumar, S. Sengupta, and B. Raj (Springer-Verlag, Berlin, 1994), p. 108.
  - <sup>35</sup>O. K. Andersen and O. Jepsen, *Phys. Rev. Lett.* **53**, 2571 (1984). We have used the latest version of the Stuttgart TB-LMTO-ASA program.
  - <sup>36</sup>O. K. Andersen, O. Jepsen, and D. Gloetzel, in *Highlights in Condensed Matter Theory*, edited by F. Bassani, F. Fumi, and M. P. Tosi (North-Holland, Amsterdam, 1985) p. 59.
  - <sup>37</sup>O. Jepsen and O. K. Andersen, *Z. Phys. B: Condens. Matter* **97**, 35 (1995).
  - <sup>38</sup>R. O. Jones and O. Gunnarsson, *Rev. Mod. Phys.* **61**, 689 (1989).
  - <sup>39</sup>P. Bagno, O. Jepsen, and O. Gunnarsson, *Phys. Rev. B* **40**, 1997 (1989).
  - <sup>40</sup>D. C. Langareth and M. J. Mehl, *Phys. Rev. Lett.* **47**, 446 (1981); *Phys. Rev. B* **28**, 1809 (1983); C. D. Hu and D. C. Langareth, *Phys. Scr.* **45**, 13244 (1992).
  - <sup>41</sup>J. P. Perdew and Y. Wang, *Phys. Rev. B* **33**, 8800 (1986); J. P. Perdew, *ibid.* **33**, 8822 (1986); J. P. Perdew and Y. Wang, *ibid.* **45**, 13 244 (1992).
  - <sup>42</sup>F. Lechermann, F. Welsch, C. Elsasser, C. Ederer, M. Faehnle, J. M. Sanchez, and B. Meyer, *Phys. Rev. B* **65**, 132104 (2002).
  - <sup>43</sup>K. Burke, J. P. Perdew, and Y. Wang, in *Electron Density Functional Theory: Recent Progress and New Directions*, edited by J. F. Dobson, G. Vignale, and M. P. Das (Plenum, New York, 1997), p. 81.

- <sup>44</sup>W. R. L. Lambrecht and O. K. Andersen, Phys. Rev. B **34**, 2439 (1986).
- <sup>45</sup>P. Bloechl, O. Jepsen, and O. K. Andersen, Phys. Rev. B **49**, 16 223 (1994).
- <sup>46</sup>D. D. Johnson, Phys. Rev. B **38**, 12 807 (1988).
- <sup>47</sup>A. D. Becke, Phys. Rev. A **38**, 3098 (1988).
- <sup>48</sup>B. K. Rao, S. R. de Biaggi, and P. Jena, Phys. Rev. B **64**, 024418 (2001); Ch. Müller, G. Seifert, G. Lautenschläger, H. Wonn, P. Ziesche, and E. Mrosan, Phys. Status Solidi **91**, 605 (1979).
- <sup>49</sup>P. A. Schultz and J. W. Davenport, J. Alloys Compd. **197**, 229 (1993).
- <sup>50</sup>J. M. Ziman, *Electrons and Phonons* (Oxford University Press, Oxford, 1960), p. 376.
- <sup>51</sup>P. Allen, in *Quantum Theory of Real Materials*, edited by J. R. Chelikowsky and S. G. Louie (Kluwer, Dordrecht, 1996), p. 219.
- <sup>52</sup>B. R. Coles, Proc. Phys. Soc. London, Sect. B **28**, 221 (1951).